JTTEE5 14:239-250
DOI: 10.1361/10599630523818
1059-9630/$19.00 © ASM International

Advanced Microstructural Characterization of Plasma-Sprayed Zirconia Coatings Over Extended Length Scales

Anand A. Kulkarni, Allen Goland, Herbert Herman, Andrew J. Allen, Jan Ilavsky, Gabrielle G. Long, and Francesco De Carlo

(Submitted September 5, 2003; in revised form April 5, 2004)

Achieving control of the microstructure of plasma-sprayed thermal barrier coating (TBC) systems offers an opportunity to tailor coating properties to demanding applications. Accomplishing this requires a fundamental understanding of the correlations among processing, microstructure development, and related TBC properties. This article describes the quantitative characterization of the microstructure of plasma-sprayed partially stabilized zirconia (PSZ) coatings by means of x-ray and neutron-scattering imaging techniques. Small-angle neutron scattering, ultra-small-angle x-ray scattering, and x-ray microtomography were used to characterize and visualize the nature and structure of the features in these material systems. In addition, the influence of processing parameters on microstructure development is discussed along with thermal cycling effects on the pore morphology, and their resultant influence of the porosity on the thermal conductivity and elastic modulus of plasma-sprayed PSZ TBCs.

Keywords elastic modulus, plasma spray, small-angle neutron scattering, thermal barrier coatings, thermal conductivity, thermal cycling, ultra-small-angle x-ray scattering, x-ray microtomography

1. Introduction

For today's advanced gas turbine and high-performance internal combustion engines, the key issue, along with operational economics and the achieving the longest possible lifetimes, is the prime reliance on the materials (Ref 1). This has spawned a considerable amount of research on various aspects of the relevant material systems, particularly on ceramic thermal barrier coatings (TBCs). Zirconia-base TBCs are widely used on the surfaces of high-temperature engine components. Their use improves the thermodynamic efficiency of the engines, because they enable higher operating temperatures and have reduced cooling air requirements. Simultaneously, they prolong substrate lifetimes due to lower temperatures at the metal surface (Ref 2-4). The microstructures and properties of TBCs are closely linked to processing technology: for example, plasma spray (PS) and electron beam-physical vapor deposition (EB-PVD) each produce distinctive microstructures and thermomechanical characteristics. Each of these processing techniques has advantages and disadvantages. The scale, performance, and cost requirements determine the choice for a particular TBC application. The research reported in the article focuses on the relationship between microstructure development and the in-service coating behavior of plasma-sprayed coatings.

Plasma spraying is a high-temperature process. The feedstock powder is fed into a plasma arc, where it is melted and accelerated to high velocities, before it impinges onto a substrate. Upon reaching the substrate, the melted powder solidifies rapidly to form "splats," or flattened particles (Ref 5-7). The deposit develops by the successive impingement of melted particles and interbonding among the splats. The product microstructure is axially symmetric when viewed along the surface normal, provided this is also the spray direction, but it is anisotropic when viewed in section (i.e., in any plane perpendicular to the substrate). This axial symmetry is used in the analysis of the x-ray and neutron scattering data. The microstructure of plasma-sprayed coatings typically includes porosity in the form of interlamellar voids (between the splats), and very fine pores and cracks within the splats resulting from thermal stress relaxation (Ref 8). It is well understood that the porosity in TBCs is a significant factor in determining TBC properties (Ref 9, 10). This is important because if the pore character and morphology within TBCs can be controlled, then the TBC properties can be tailored to specific applications. This is the governing principle in designing TBCs. Achieving control of the product microstructure and the coating system properties requires research aimed at understanding the correlations among processing, microstructure development, and the associated TBC properties. Until now, it has been difficult to obtain an adequate three-dimensional (3D) characterization of the microstructure. Techniques such as image analysis require reliable and reproducible cross-sectional images, and may depend on image acquisition conditions and threshold selection for the porosity (Ref 11, 12). Even when image analysis is successful, it delivers two-dimensional (2D) information; it may not yield compositional information, and images with poor contrast may give rise to errors. In the research reported here, x-ray and neutron-scattering imaging techniques

Anand A. Kulkarni, Allen Goland, and **Herbert Herman,** University at Stony Brook, Stony Brook, NY, 11794; **Andrew J. Allen, Jan Ilavsky,** and **Gabrielle G. Long,** National Institute of Standards and Technology, Gaithersburg, MD, 20899; and **Francesco De Carlo,** Advanced Photon Source, Argonne National Laboratory, Argonne, IL, 60439. Contact e-mail: anandk013@gmail.com.

are used to provide a statistically rigorous 3D characterization of the porous microstructure of initial and in-service (i.e., thermally cycled) TBCs. Ultimately, the goal is to provide a quantitative comparison of PS and EB-PVD microstructures in the expectation that such information will lead to an improved understanding of the relationships among processing, microstructure, and the resultant properties of these important materials.

Thus, the primary aim of this investigation was to examine the effect of processing parameters on the microstructural development, which, in turn, affects the properties of partially stabilized zirconia (PSZ) coatings with 7 to 8% mole fraction yttria. The parameters investigated were: the feedstock particle size; the in-flight particle state; and substrate conditions such as the temperature and angle-of-impact of the melted particle. The droplet-substrate interaction was also investigated through single-splat observations, and the splat-splat interactions were also followed because these lead to the microstructure development. Correlations between the measured microstructure and properties of the coatings have been characterized. Finally, results are presented on the changes in microstructure and the properties that occur as a result of thermal cycling. The methods used for microstructural characterization included small-angle neutron scattering (SANS), ultra-small-angle x-ray scattering (USAXS), and imaging by means of computed x-ray microtomography (XMT). Quantitative information on microstructural features with respect to porosity, dimensions, pore size distribution, and orientation was sought using scattering techniques. X-ray microtomography offers 3D images of open and closed porosity, along with information on the surface area, size, and position of the particles, with limited resolution.

2. Experimental Techniques

The studies presented in the article focus on gaining a systematic understanding of the influence of processing on microstructure development in plasma-sprayed coatings. The influence of the feedstock particle size, the in-flight particle state, and substrate conditions, such as temperature and angle-of-impact of the melted particle, on the splat morphology and coating microstructure were studied. To do this, a fully quantitative microstructure characterization was carried out for both as-sprayed and thermally cycled coatings. Individual splats were collected on polished stainless steel substrates, and coatings (0.75 mm thick) were deposited on mild steel using a Sulzer Metco* (Winterthur, Switzerland)3MB plasma gun at a 100 mm standoff distance. The spray parameters are listed in Table 1. A preliminary microstructural evaluation of the coatings was carried out using optical microscopy and scanning electron microscopy (SEM). Some of the coatings (both on steel and bond-coated superalloy substrates) were then subjected to 10 cycles of heating at 1150 °C for 30 min, followed by cooling in air for 15 min.

Freestanding coatings, which had been removed from the substrate, were used for porosity characterization, thermal conductivity measurements, and SANS studies. The dimensions of the samples were 5 × 10 × 0.75 mm for the porosity measurements and 1.5 × 7 × 0.75 mm for SANS measurements. For the USAXS, XMT, and modulus measurements, the coating was measured on the substrate. The coatings were thinned (0.25 mm) in cross section for x-ray transmission for USAXS and XMT studies. The central goal of these studies was to gain a comprehensive understanding of the nature of porosity in these PSZ coatings. Various aspects of the porosity were measured by different techniques. Surface-connected porosity was measured by means of mercury intrusion porosimetry (MIP) using a Quantachrome (Boynton Beach, FL) Autoscan 33* porosimeter. Even though XMT measures both the open and the closed porosity, the spatial resolution of our current XMT facility limits the detection of the smaller-scale pores in the system. Therefore, the most reliable determination of the total porosity content was obtained using the precision density (PD) method, where mass-to-volume ratios were obtained for a cut rectilinear specimen. This technique yields the density as a percentage fraction of the theoretical density (TD), where a fully dense, pore-free sample is the 100% TD. The uncertainty in the measured density has an SD of ±0.1% TD, based on the average of 10 measured identical specimens. The assumed TD was 6 g/cm^3.

Table 1 Processing parameters

Plasma gun	Sulzer Metco 3MB
Current	650 Å
Voltage	66-68 V
Primary gas	40 SLM Ar
Secondary gas	8 SLM H2
Carrier gas	3000 SCCM Ar
Feed rate	20-40 g/min
Standoff distance	100 mm

3. Thermal and Mechanical Property Measurements

Thermal conductivity measurements were made on a 12.5 mm (0.5 in.) diameter disk, which was coated with carbon, using a laser-flash thermal diffusivity instrument (Netzsch Corporation, Boston, MA). Elastic modulus measurements performed by means of depth-sensitive indentation measurements, were carried out with a Nanotest 600 instrument (Micromaterials Inc., Cambridge, UK) with a 1.59 mm (1/16 in.) WC-Co spherical indenter with a maximum load of 10 N. Both in-plane and out-of-plane elastic modulus measurements were carried out to examine the anisotropy in the coatings. The instrument enables a basic load-displacement curve to be obtained, or multiple partial load-unload cycles to be performed. This allows hardness and elastic modulus values to be measured as a function of the load-contact stress. The indentation procedure consisted of 10 to 15 loading-unloading cycles. The load-displacement records were evaluated based on the Oliver and Pharr method in which the elastic modulus was determined from the elastic recovery part of the unloading curve.

4. Small-Angle Neutron Scattering

Small-angle neutron scattering studies were carried out using a 30 m SANS instrument at the Cold Neutron Research Facility at the National Institute of Standards and Technology (NIST),

*Specification of the commercial apparatus is given for completeness; it does not imply NIST endorsement, nor does it indicate that it is optimal for the purposes for which it was used.

Gaithersburg, MD. A monochromatic beam of cold neutrons passes through the specimen in transmission geometry, and the scattered neutrons are recorded on a 2D detector. The details of the experiment have been described elsewhere (Ref 13-15). The voids and grains within the sample have different neutron-scattering-length densities (ρ), causing a small component of the incident beam to be scattered. The SANS experiments comprise two types of measurements, with the first being anisotropic Porod scattering. In Porod scattering, the terminal slope of the small-angle-scattering curve is used to determine the surface area of the scatterers (voids or pores in this case) in the sample. If the neutrons pass through a TBC section, which is cut perpendicular to the surface plane so that the surface area is distributed anisotropically around the incident beam direction, the variation in the intensity of the terminal slope with sample and beam orientation can be related to the anisotropic void surface area distribution. Upon averaging the Porod scattering over all sample orientations, the total void surface area per unit sample volume is obtained, independent of the void morphology. Because small objects have a larger surface-to-volume ratio than large ones, the smaller voids in the microstructure are the dominant contributors to the total surface area. The second type of measurement is anisotropic multiple SANS (MSANS). In MSANS, beam broadening as a function of neutron wavelength is used to determine the size of the scatterers (again, the voids). In anisotropic MSANS, the beam-broadened profile radius of curvature (r_c) versus wavelength is measured for two sample orientations: (a) with the incident neutron beam in the spray direction and $\boldsymbol{Q}$ (scattering wave-vector) in the substrate plane; and (b) with the incident neutron beam perpendicular to the spray direction and $\boldsymbol{Q}$ in a plane perpendicular to the substrate. These data yield information on the microstructural anisotropy. The sector-averaged anisotropic MSANS ($\boldsymbol{Q}$ out-of-plane) data also provide microstructural orientation information, as has been discussed elsewhere (Ref 13, 14).

In Porod scattering, the scattering intensity, $I(\boldsymbol{Q})$, is a function of both the magnitude and the direction of the scattering vector, $\boldsymbol{Q}$, and its orientational average, $\langle I(\boldsymbol{Q})\rangle$ is given by:

$$\langle I(\boldsymbol{Q})\rangle \approx \frac{2\pi|\Delta\rho|^2 S_v}{\boldsymbol{Q}^4} \quad \text{(Eq 1)}$$

where, $|\boldsymbol{Q}|=[4\pi/\lambda]\sin\theta$, 2θ is the scattering angle, λ is the wavelength, S_v is the total surface area per unit sample volume, and $|\Delta\rho|^2$ is the scattering contrast between the voids and the solid matrix.

Additional microstructural information is obtained by combining MSANS information from different sample orientations, the anisotropic Porod surface area results, and PD measurements of the total porosity. A three-component void model, which includes interlamellar pores, intrasplat cracks, and globular pores, was used to obtain quantitative information regarding the porosities, sizes, and orientation distributions within each component. To interpret the anisotropic MSANS beam-broadening data, the interlamellar pores and intrasplat cracks were modeled by oblate spheroids, each with a fixed aspect ratio (β), while the globular pores are assumed to be spheres. Because the cracks are generally finer than the interlamellar pores, the aspect ratio for the cracks is set to a smaller value (more oblate) than for the interlamellar pores.

The following four constraints are imposed in the model analysis within the limits set by the experimental uncertainties (Ref 13, 14):

1. The sum of the component porosities must be equal to the total porosity obtained from PD measurements.
2. The sum of the component surface areas must be equal to the total surface area obtained from the orientationally averaged anisotropic Porod scattering.
3. The circularly averaged MSANS beam-broadening model predictions versus the wavelength model predictions must be consistent with the experimental data for both sample orientations: with the incident beam parallel to the spray direction, and with the incident beam in the plane of the substrate.
4. The predicted MSANS anisotropy must be consistent with that observed with the incident beam in the plane of the substrate.

Making use of these constraints, one can determine the volume-weighted mean opening dimensions of the intrasplat cracks and interlamellar pores, their approximate orientation distributions with respect to the spray direction, together with the mean diameter of the globular pores. The component porosity and surface area contributions may also be distinguished.

5. Ultra-Small-Angle X-Ray Scattering

Ultra-small-angle x-ray scattering studies were carried out on the UNICAT beam line 33-ID at the Advanced Photon Source at Argonne National Laboratory in Argonne, IL. This instrument uses Bonse-Hart-type double-crystal optics (Ref 16) to extend the range of small-angle x-ray scattering to very small scattering vectors ($\boldsymbol{Q}$). In small-angle scattering studies (i.e., SANS and USAXS), the structural information is always measured along the direction of $\boldsymbol{Q}$. This fact may be used to advantage with anisotropic microstructure characterization. In a modified form of the standard USAXS experiment, an x-ray beam that has been prepared using horizontally and vertically diffracting crystals is incident on the specimen in transmission geometry. Use of orthogonal diffracting crystals removes the intrinsic slit-smeared geometry of the standard USAXS experiment. The scattered intensity is measured as the crystal analyzer is rotated, so that the Bragg condition is met only for x-rays scattered at a given $\boldsymbol{Q}$. The details of the experiment have been described elsewhere (Ref 17). The x-ray energy was 17 keV ($\lambda = 0.073$ nm) to ensure adequate transmission through the highly absorbing PSZ coatings. Two methods for measuring the anisotropic USAXS were used. In the first method, the scattered intensity was measured as a function of $\boldsymbol{Q}$ for each orientation of the azimuthal angle α. In the second, the scattered intensity at a particular $\boldsymbol{Q}$ was measured as a function of α by rotating the sample about the center of the x-ray beam. The anisotropies in the scattering at different values of $\boldsymbol{Q}$ are related to the anisotropies of the microstructure at different length scales, thus providing a series of anisotropy maps as a function of the scattering feature size.

6. X-Ray Computed Microtomography

The XMT studies were carried out on the XOR 2-BM beam line at the Advanced Photon Source. The experimental details and setup have been described elsewhere (Ref 18, 19). In this

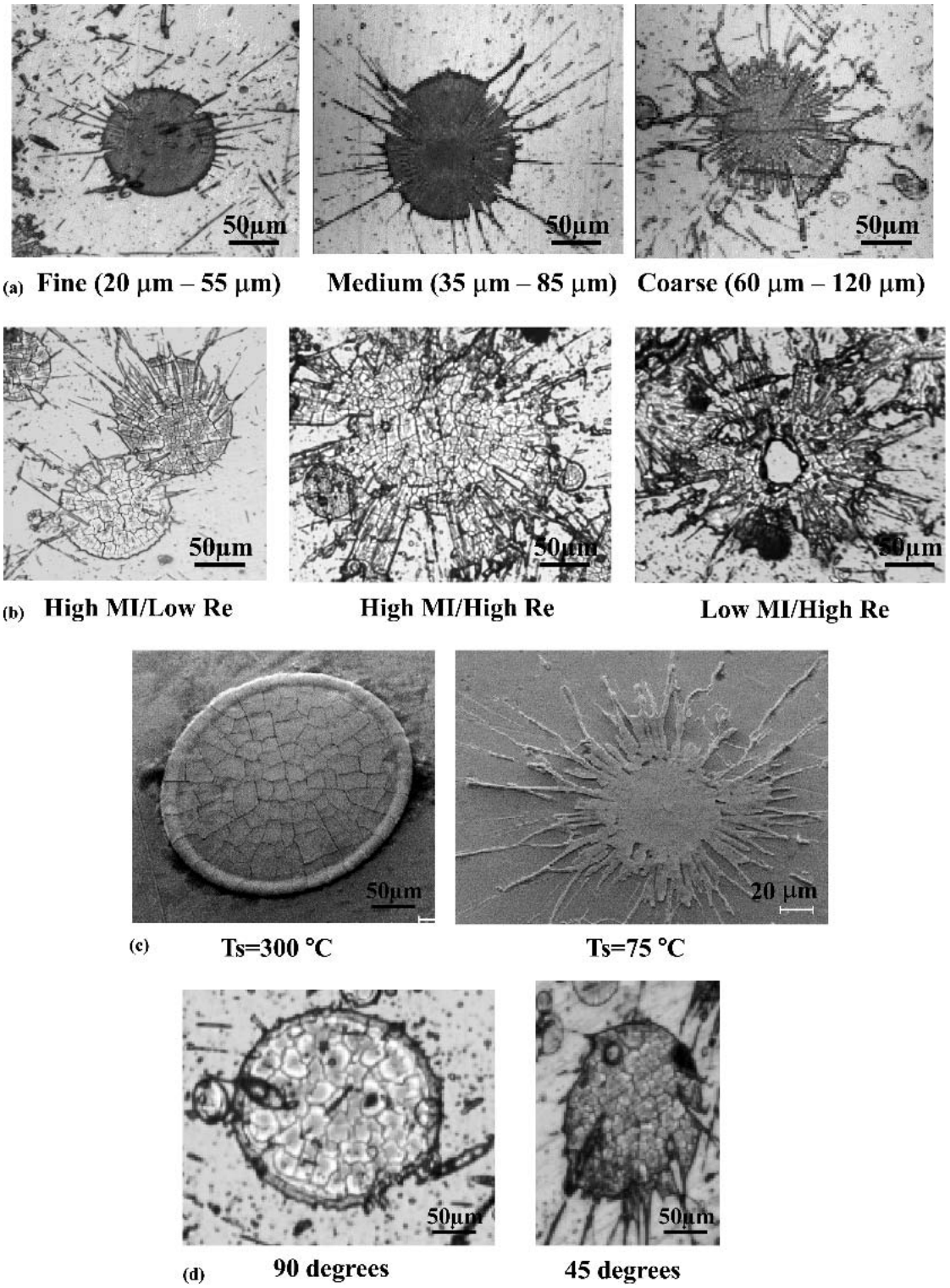

Fig. 1 Influence of processing parameters on splat morphologies: (a) feedstock characteristics (particle size); (b) in-flight characteristics (particle state); (c) substrate conditions (substrate temperature [Ts]); and (d) angle-of-impact effects

experiment, a large-area, collimated x-ray beam traverse the sample, and the transmitted x-rays are recorded on an area detector. For the TBC samples, the image is an x-ray attenuation map of the sample. Images are recorded at discrete angular intervals (typically in 1/4° steps) as the sample is rotated for a total of 180° about the vertical axis perpendicular to the incident X rays. In addition to the 720 2D attenuation maps, "dark-field" images (i.e., background measurements with the x-rays off) and

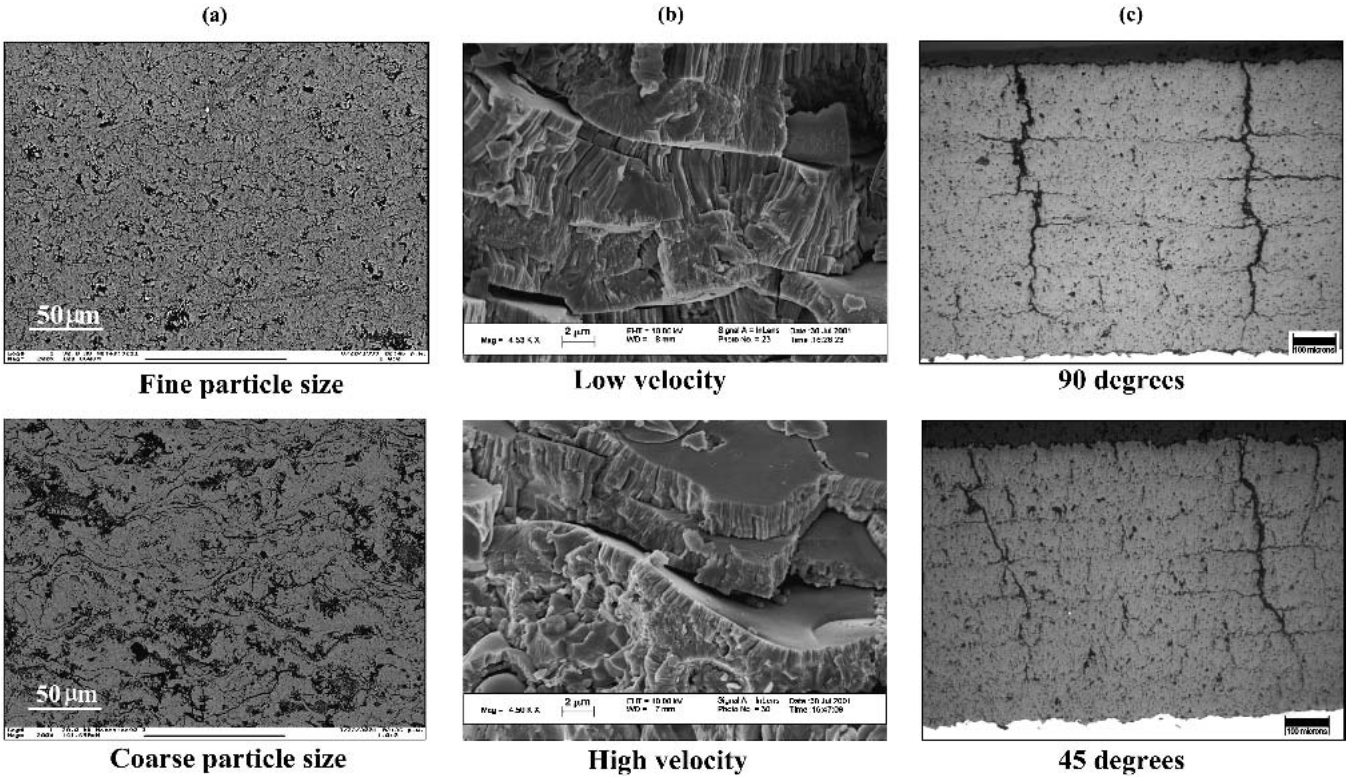

Fig. 2 Influence of processing parameters on coating microstructures: (a) feedstock (particle size); (b) particle state (particle velocity); and (c) substrate (angle-of-impact). A coarse feedstock gives high porosity, but a high particle velocity gives thinner splats (and a large number of splat interfaces). Some preferential orientation of macrocracks occurs toward the spray direction when the angle-of-impact is not 90°.

"white-field" images (i.e., x-rays used for measurements, with no sample in the beam) are acquired. These images are necessary for normalizing the 2D projection images. The normalized images are then aligned to ensure that the rotation axis is accurately located at the center of the images. The data are reconstructed using a filtered back-projection algorithm and are then stacked to build 3D images of the microstructural features. While the pixel size (image resolution for software thresholding) was 1.3 μm, this does not represent the minimum pore size that can be resolved. Realistically, the pore has to be larger than this size at least in one dimension to be recognizable. The resolution of the final reconstruction is limited by the resolution of the absorption images, which is related to x-ray energy, the properties of the scintillator screen, and visible-image optical magnification. The technique provides volumetric information on microstructure distribution by mapping 3D x-ray coefficients through the sample.

For the analysis of the x-ray tomographic data, 3D medial axis transforms are used to obtain quantitative information on porosity and its variation with thickness (Ref 20). The medial axis transform is a dimensional reduction of an object to its skeletal remnant, preserving information on the extent and connectivity of the original object. Intuitively, a medial axis is the skeleton of an object along its geometric middle (i.e., a point for a sphere and a line along the center for a cylinder). The analysis involves thresholding an overlapping bivariate-mapped distribution of attenuation coefficients (i.e., tomographic raw images) to obtain segmented (i.e., black-and-white) images. This is followed by the construction of the medial axis with an iterative erosion procedure (Ref 21) to trace the fundamental geometry of the void pathways. Information on porosity, pore size distribution, and connectivity is obtained using numerical algorithms, the details of which have been presented elsewhere (Ref 20).

7. Results and Discussions

7.1 Microstructure Development

In this section, the spray droplet/substrate interactions are described because these govern the microstructure development of the coating. The intrinsic properties of the individual splats and the intricate correlations among them are affected by the in-flight feedstock-particle properties within the plasma (i.e., their temperature, velocity, size, degree of melting, and extent of particle-particle interaction) as well as the substrate conditions (i.e., its degree of wetting, thermal contact resistance, roughness profile, chemical interactions, and extent of modification by prior deposition of splats). The governing interrelations of droplet impact and subsequent solidification history of the process parameters and the substrate conditions are examined here.

Figure 1 shows the role of the processing parameters on the splat (single-particle) morphology. The figure displays the different splat morphologies observed for the three different particle sizes. It is evident that the morphology of the splats changes from a disk-like shape to a fragmented shape with increasing particle size. The shapes shown are representative of typical

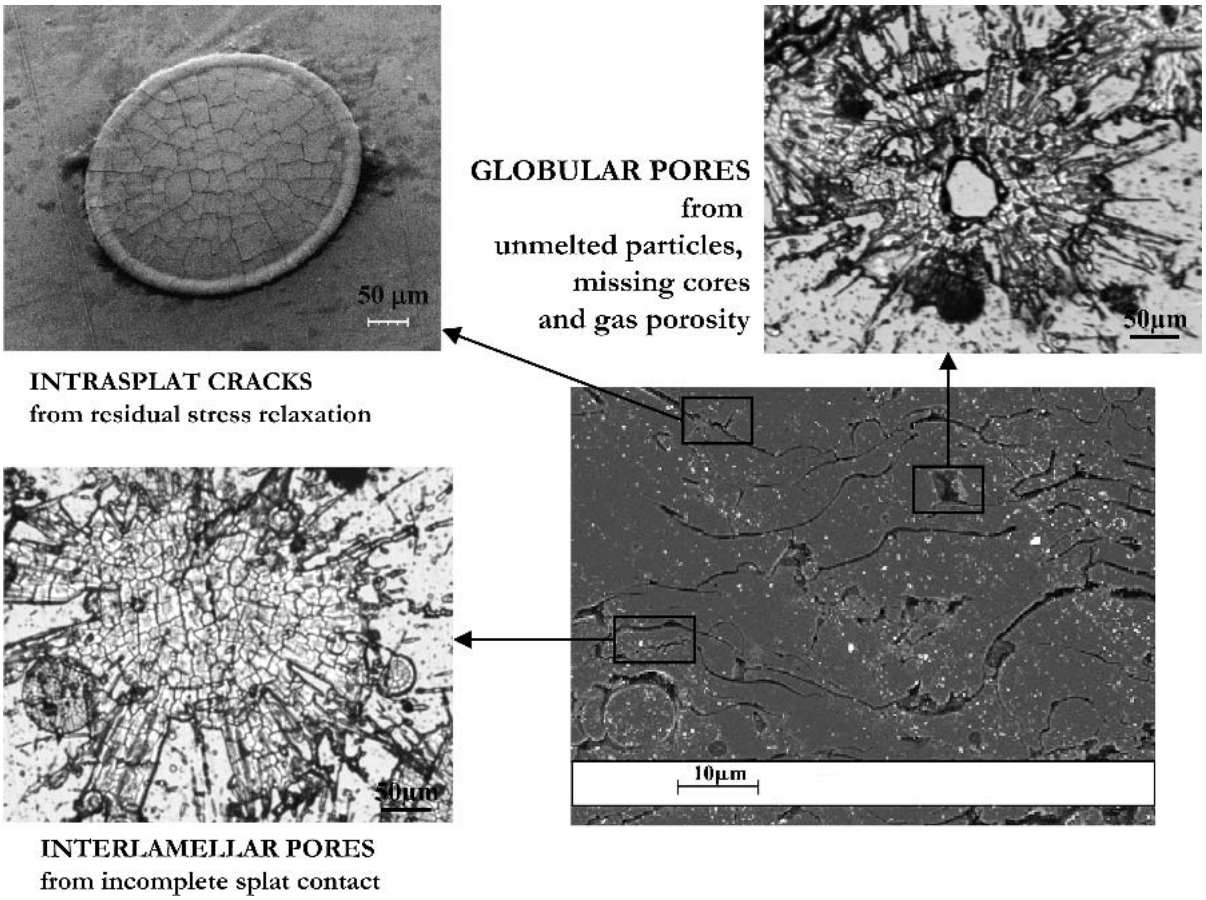

Fig. 3 Association of the pore features with single-splat morphologies observed in a plasma-sprayed PSZ coating

splats for each size distribution. The splats were quantified using a dimensionless parameter called the *fragmentation index* (FI). This parameter was calculated as the ratio of the total area of the fragmented (splashed) splat divided by the area of its contiguous part:

$$\mathrm{FI} = A_{\mathrm{total}}/A_{\mathrm{splat}} = (R_{\mathrm{total}}/R_{\mathrm{splat}})^2 \qquad \text{(Eq 2)}$$

where R is a dimension such as the radius. For a circular (non-fragmented) splat, the value of the FI equals one. The fragmentation indexes deduced from the optical images of the splats in Fig. 1 were 2.50, 2.80, and 9.10, respectively, for the fine, medium, and coarse powders.

Also shown in Fig. 1 is the influence of in-flight particle characteristics on the splat morphology. In-flight particle size and temperature were monitored using a Tecnar DPV2000* thermal-spray-diagnostic instrument. Vaidya et al. (Ref 22) proposed using a coupled parameter, called the *melting index* (MI), to describe the particle state that is defined by the particle temperature, velocity, size, and dwell time. Another parameter that describes the particle kinetic state is the Reynolds number (Re), which is defined as the ratio [$D_p v\rho$ to μ], where D_p, v, ρ, and μ are, respectively, the molten particle diameter, velocity, density, and viscosity. The splat morphologies show that the condition combining a high MI with a low Re describes highly molten particles traveling with low velocity, resulting in less particle fragmentation upon impact, producing disk-shaped splats. However with, increasing Re, the splats fragment, and the morphologies depend on the molten state of the particles. It is observed that the condition with low MI and high Re produces splats with a missing core. Another parameter that has significant influence on the splat morphology is substrate temperature. A higher substrate temperature results in better wetting and adhesion, and disk-shaped splats form rather than the fragmented splats that form with a low substrate temperature. Finally, the angle-of-impact effects are shown, in which the splats are disk-shaped for normal incidence and elongated for the 45° impact angle. These distinct morphologies certainly influence microstructure development.

The microstructures of coatings, as a function of feedstock particle size, particle velocity, and angle of impact are presented in Fig. 2. The coating prepared from the fine powder shows well-adhered splats, with a few interlamellar pores. The coating prepared from the coarse powder, on the other hand, shows poorly adhered splats and a significant number of large pores. This is due to the existence of fragmented splats with poor splat-to-splat contact, larger interlamellar pores, and larger areas of polishing pullouts. The figure also compares microstructural features resulting from low and high particle velocities. The coating sprayed at low velocity shows well-adhered splats, compared

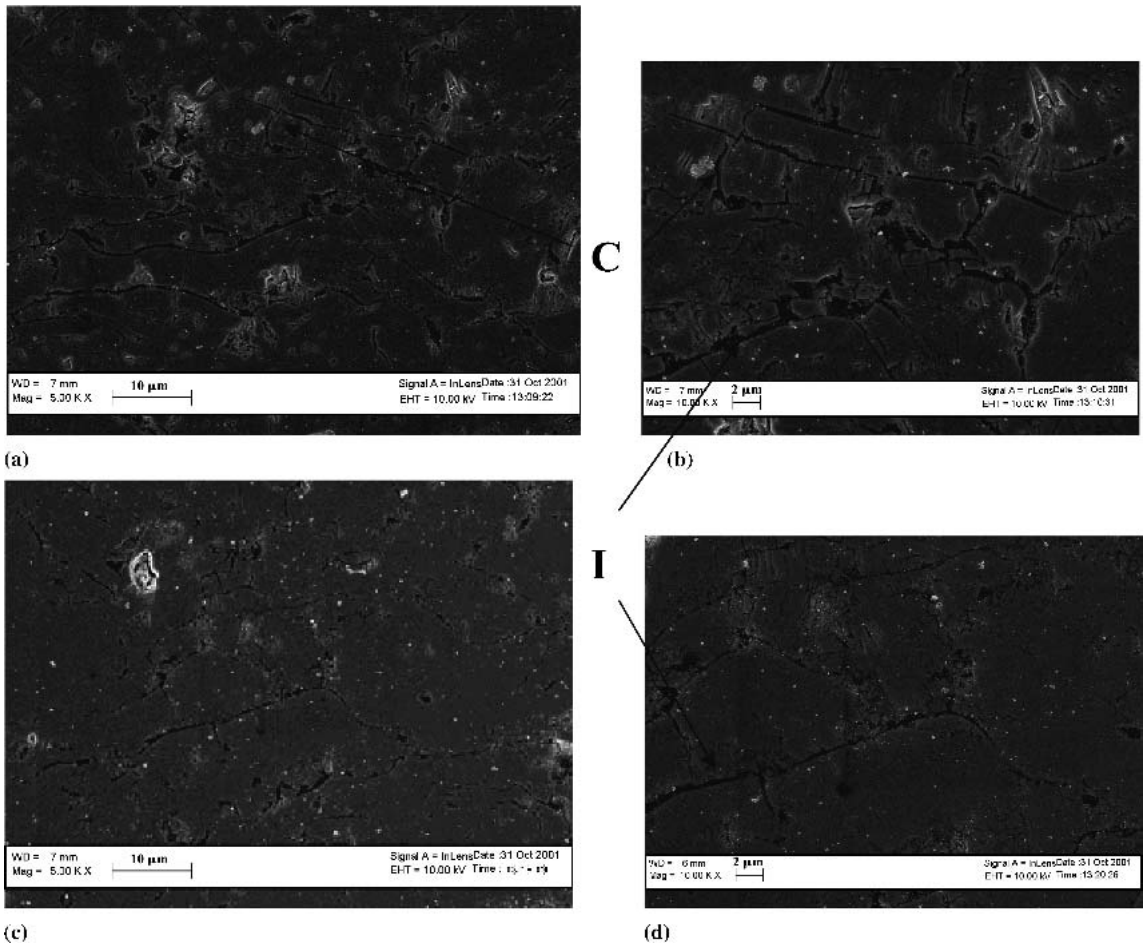

Fig. 4 Back-scattered SEM images showing microstructures for (a) an as-sprayed coating with (b) a high-magnification image, and (c) a thermally cycled coating with (d) a high-magnification image. I, interlamellar pores; C, intrasplat cracks

Table 2 Property measurements of as-sprayed and thermally cycled coatings (10 cycles at 1150 °C/30 min heating + 15 min cooling)

Coating	MIP porosity, %	Thermal conductivity, W/(M ± K)	Out-of-plane elastic modulus, GPa	In-plane elastic modulus, GPa
Steel				
As-sprayed	10.5 ± 0.3	1.2 ± 0.1	30.0 ± 1	41.4 ± 1
Thermally cycled	9.0 ± 0.5	1.8 ± 0.3	34.4 ± 4	35.5 ± 2
Superalloy				
As-sprayed	6.0 ± 0.3	1.7 ± 0.3	29.0 ± 1	37.4 ± 2
Thermally cycled	5.4 ± 0.3	… (a)	47.4 ± 2	47.0 ± 4

Note: Values given as mean ± SD.
(a) Sample broke; hence, it could not be measured.

with that sprayed at high velocity. Also, the thickness of the splats is different; the low-velocity condition results in thicker splats than the high-velocity condition, and thus there are fewer interfaces in the former case than in the latter case. The microstructures for the angle-of-impact studies show segmented crack networks due to the biaxial stress developed during deposition at high power and particle flux. Earlier work on the effect of spray angle on gray alumina coatings showed the tendency for cracks to orient preferentially with the spray direction (Ref 23). This surprising effect is seen for PSZ coatings (tougher than alumina), showing cracks tilted by 70° to 80° to the substrate plane for the substrate inclined 45° from the spray angle. A detailed study of porosity-property correlations for these conditions has been presented elsewhere (Ref 24).

Figure 3 offers some insights into microstructure development by showing the three types of void systems that have been identified in these ceramic coatings. The intrasplat cracks result from the relaxation of residual stresses that developed due to

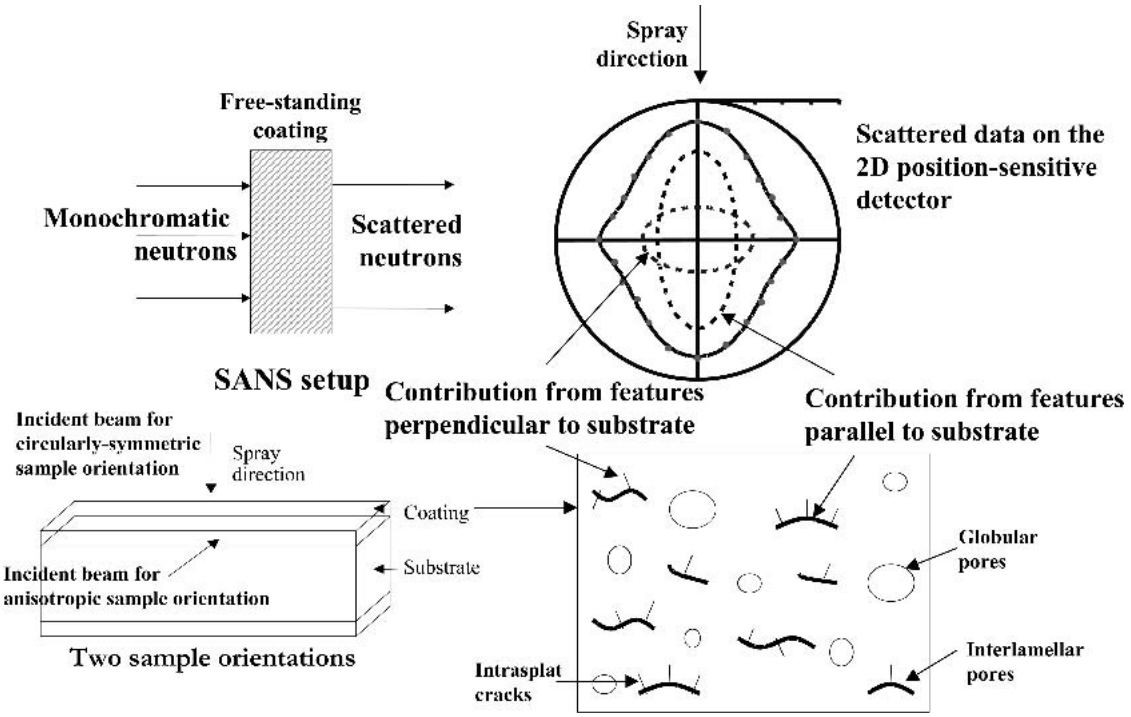

Fig. 5 Schematic of the SANS measurement geometry and the microstructure feature contributions to the anisotropic scattering

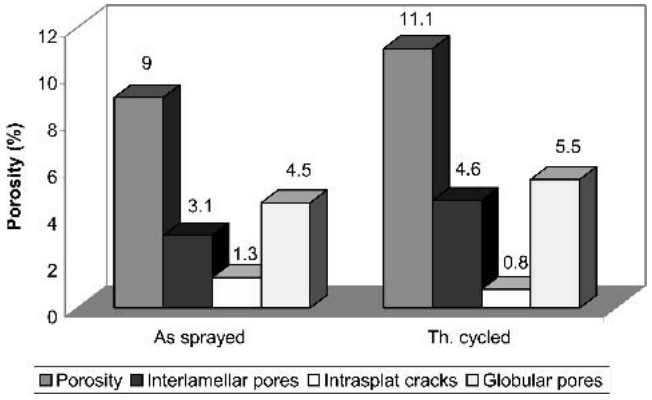

Fig. 6 Quantitative separation of the coating porosity into the microstructural components

constrained shrinkage of a solidifying splat. The interlamellar pores result from particle fragmentation that causes poor wetting/adhesion between the splats. The globular pores result from a lack of filling around the undulation of the splats as well as from the existence of missing core due to incomplete melting of the particle in the flame.

7.2 Porosity Characterization and Thermal Cycling Effects

This section presents a case study in which quantitative microstructural characterization is carried out on initial and aged coatings to trace the changes that take place upon thermal cycling. The coatings were deposited either onto mild steel or onto bond-coated superalloy substrates. Upon high-temperature exposure at 1150 °C, the coating on the steel substrate abruptly

Table 3 Quantitative multiple small-angle neutron scattering results with orientation information

		Component porosity, %						
Coating	Porosity, %	Interlamellar pores	Intrasplat pores	Globular pores	Opening dimensions, μm	Globular pore diameter, μm	Cracks, %	Pores, %
As-sprayed	9.0 ± 0.3	3.1 ± 0.5	1.3 ± 0.5	4.5 ± 0.2	0.047 ± 0.005	0.30 ± 0.03		
0°-30°							0.8	92.6
30°-60°							17.9	6.9
60°-90°							81.3	0.5
Thermally cycled	11.1 ± 0.4	4.6 ± 0.6	0.8 ± 0.9	5.5 ± 0.5	0.051 ± 0.006	0.30 ± 0.04		
0°-30°							3.8	99.0
30°-60°							25.8	0.73
60°-90°							70.4	0.27

Note: Values given as mean ± SD, unless otherwise indicated.

debonded, while that on the superalloy substrate remained intact. This difference was attributable to the different coefficient of thermal expansion (CTE) mismatches in the two cases as well as poor oxidation resistance of steel at 1150 °C.

Cross-sectional SEM micrographs of the as-sprayed and thermally cycled coatings are presented in Fig. 4, in which 4(a) shows a typical plasma-sprayed coating with a layered structure. The interlamellar porosity, resulting from poor adhesion between the splats, is evident. The inset of Fig. 4b (the high-magnification image) reveals the presence of microcracks. Figure 4(c) shows a dense coating microstructure after thermal cycling, and Fig. 4(d) (the high-magnification image) shows that the microcracks have sintered upon heating.

Table 2 presents coating property results for an as-sprayed coating on steel, a thermally cycled coating on steel, an as-sprayed coating on a superalloy, and a thermally cycled coating on a superalloy. The porosity, measured using MIP, thermal conductivity, and elastic modulus values, is given for the PSZ coating in each case, together with the estimated SDs. The table shows that the thermal conductivity of the as-sprayed coatings is significantly different for the coatings sprayed on different substrates. In-plane and out-of-plane measurements indicate the degree of anisotropy in each coating. The out-of-plane elastic modulus values (made in the through-thickness direction) are not significantly different between the coatings, but the in-plane values (made on the cut cross section) are some 15% different. Upon thermal cycling, the thermal conductivity increases for the one coating that was measured (the free-standing form of the coating off the bond-coated superalloy substrate broke). The influence of CTE mismatch between the coating and the substrate is evident in the modulus values. The out-of-plane modulus (measured on the top surface) increases for both coatings, due to sintering of the interlamellar pores. The in-plane modulus, which is sensitive to the crack networks, exhibits a different behavior. Due to CTE mismatch between steel and zirconia, and the severe oxidation of the steel substrate, cracks open on heating, and the modulus decreases. However, with the superalloy substrate, the lower CTE mismatch between the bond coat and the top coat leads to crack sintering and, hence, to an increase in the elastic modulus. Further insight into the porosity-property relationship is sought using scattering techniques.

7.3 Small-Angle Neutron Scattering Results

This section presents SANS results for the coatings deposited on the superalloy substrates in their as-sprayed and thermally cycled conditions. Figure 5 recalls the experimental beam geometry, and indicates how the different anisotropic distributions of intrasplat cracks and interlamellar pores contribute to the (Porod) scattering for the anisotropic sample orientation. The results from a quantitative separation of microstructural features into their components, which was obtained from the MSANS model analysis, are presented in Fig. 6 and Table 3. Information on the component porosities, their mean opening dimensions, and the approximate orientation distributions of the three void populations, which were obtained by satisfying all of the constraints in the MSANS model, are listed in Table 3 with their estimated standard uncertainties. Approximate anisotropic orientation distributions of the intrasplat cracks and the interlamellar pores, which were derived from the MSANS model, are also shown in Table 3. The orientation distributions for the interlamellar-pore spheroidal elements with 1-to-5-aspect ratio and the intrasplat-crack elements with 1-to-10 aspect ratio are separately parameterized, such that the intrasplat cracks are found to be predominantly perpendicular to the substrate (spheroidal-elements normal cracks 60° to 90° from the spray direction), and the interlamellar pores are found to be predominantly parallel to the substrate (spheroidal-elements normal cracks 0° to 30° from the spray direction).

The results in Table 3 indicate that the total porosity measured by the PD method increases upon thermal cycling. Table 3, however, shows the component porosity of intrasplat cracks decreasing for the thermally cycled case, owing to sintering.

7.4 Ultra-Small-Angle X-Ray Scattering Results

The USAXS studies of the as-sprayed and the thermally cycled coatings are presented in Fig. 7, which shows the quan-

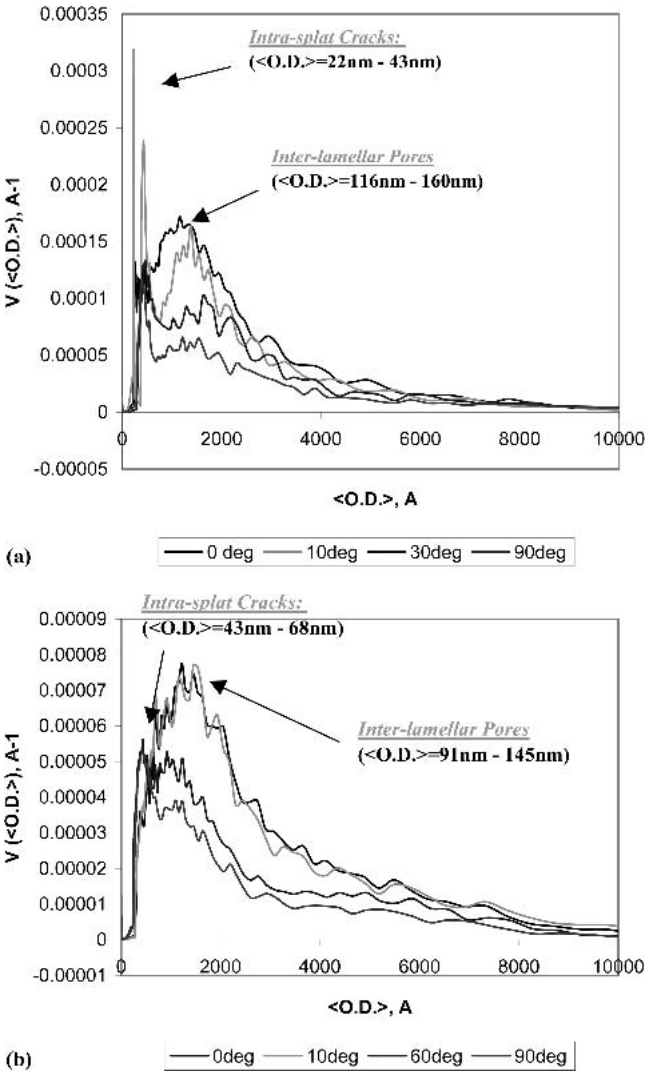

Fig. 7 MAXENT void volume fraction size distributions, V(<O.D.>), for given directions of $\boldsymbol{Q}$ with respect to the spray direction: (a) as-sprayed coating; and (b) thermally cycled coating

titative volume distributions of the intrasplat cracks and the interlamellar pores for the two coatings. The crack and pore volume size distributions were derived from the USAXS intensity versus $\boldsymbol{Q}$ curves using the maximum entropy-fitting routine, MAXENT (Ref 25). The calculated size distributions assume random orientation distributions of the cracks and interlamellar pores. However, despite the anisotropy observed, the basic trends are still apparent. The results indicate that both intrasplat cracks and interlamellar pores are present in the as-sprayed coating (Fig. 7a), whereas the interlamellar pores dominate the microstructure in the thermally cycled coating (Fig. 7b). These results are consistent with the microscopy data. The size ranges of the intrasplat cracks and interlamellar pores are marginally different for both systems. The analysis shows the opening dimension for interlamellar pores to be between 116 and 150 nm, and that for the intrasplat cracks to be between 22 and 43 nm. The aspect ratio was assumed to be 1 to 10 for both cases. Upon thermal cycling, the opening dimension for interlamellar pores decreases to between 91 and 145 nm, and that for the intrasplat cracks increases to between 43 and 68 nm. This increase in size can be attributed to CTE mismatch between the coating and substrate upon heating. However, it should be noted that the $\boldsymbol{Q}$ resolution of the USAXS instrument limits the detection of void sizes to those below 1.5 μm in radial diameter.

7.5 X-Ray Microtomography Results

The raw data collected as cross-sectional maps are reconstructed using the fast-Fourier transform algorithm, based on the so-called *Fourier slice* theorem, which is used to generate individual 2D slices. These slices were normalized and centered to generate sinograms (grayscale density maps). Figure 8 shows three such images, revealing the variation of porosity with thickness. These grayscale images depict bimodal peaks in the histogram of the linear attenuation coefficient; one is due to the voids, and the other is due to the solid material. This histogram allows threshold attenuation values to be selected for porosity calculations. Figure 9 shows reconstructed 3D images of the coating microstructures, in which the void space is displayed as transparent. Void features are evident in both the as-sprayed coatings and in the thermally cycled condition. The reconstructed images show a predominantly globular porosity due to the resolution limit of the XMT facility.

The procedure to obtain the results of the 3D medial axis analysis carried out on these images was as follows. First, the 2D images were converted from grayscale density to "black-and-white" images by a process of segmentation, involving population assignment (material and pores) for each voxel in the image. Because the pore-grain boundary in the image is "fuzzy" due to the finite voxel resolution and the image-collection noise, a localized thresholding procedure, based on the indicator-kriging algorithm (Ref 21), was used. These segmented images are then treated using a mathematical erosion algorithm, for example, to construct the medial axis (skeleton) of the void space, and to obtain geometric information on the specific surface area and the distribution of volumes of disconnected components. The porosities, which are measured by a straight voxel-voxel count of black-and-white regions in the segmented images, are presented in Fig. 10. Each individual point in Fig. 10 is a volumetric average of 10 slices in the coating. Also the SD for each point is about 1% to 2%, which is unnoticeable on the graph. Thus, the variation in porosity with depth, which was observed in the as-sprayed case, reflects changes in the splat-void microstructure that occurred as different layers were deposited. Much of this

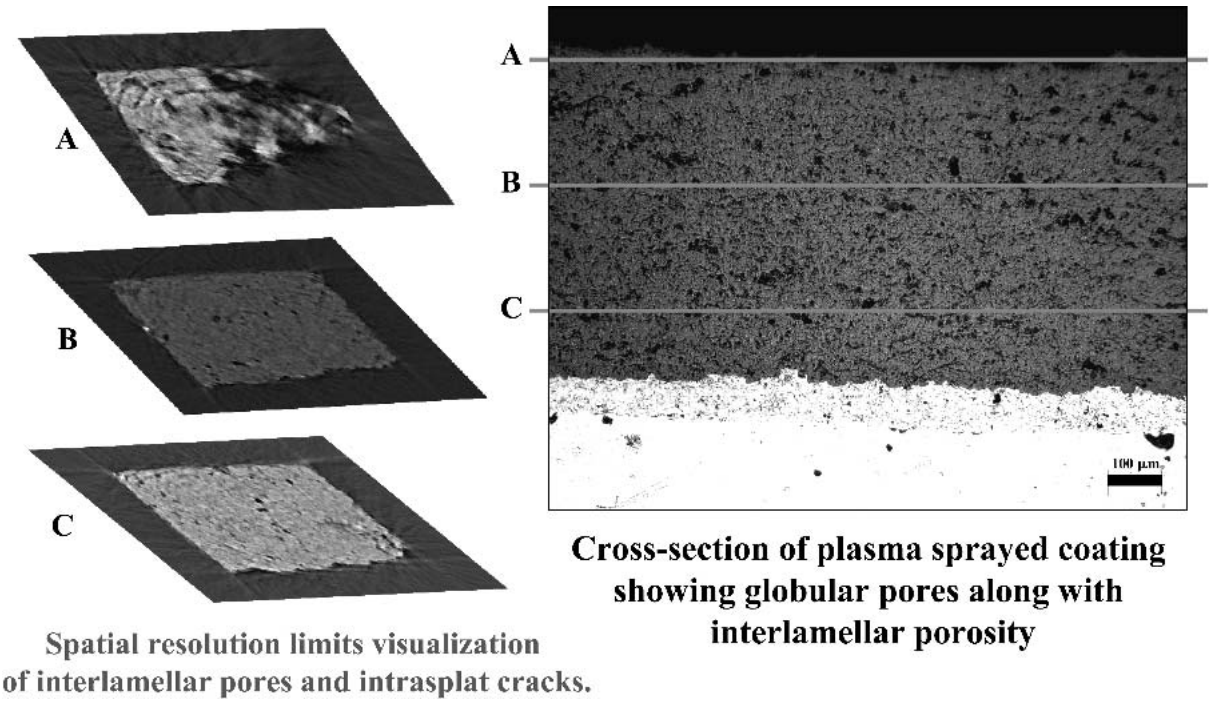

Fig. 8 Raw XMT images showing the variation in coating porosity through the thickness

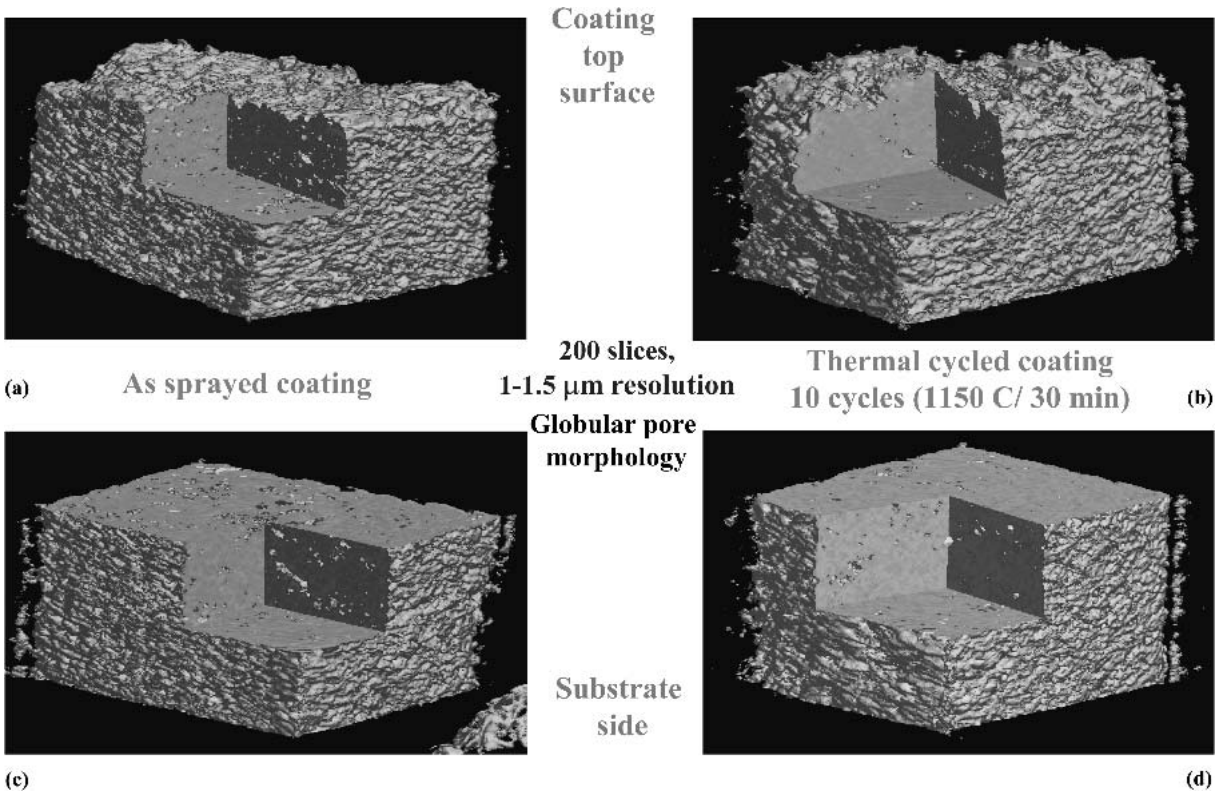

Fig. 9 Three-dimensional XMT image reconstruction of TBC microstructures showing globular porosity at 1.3 μm resolution. Some sintering is observed in the thermally cycled coating.

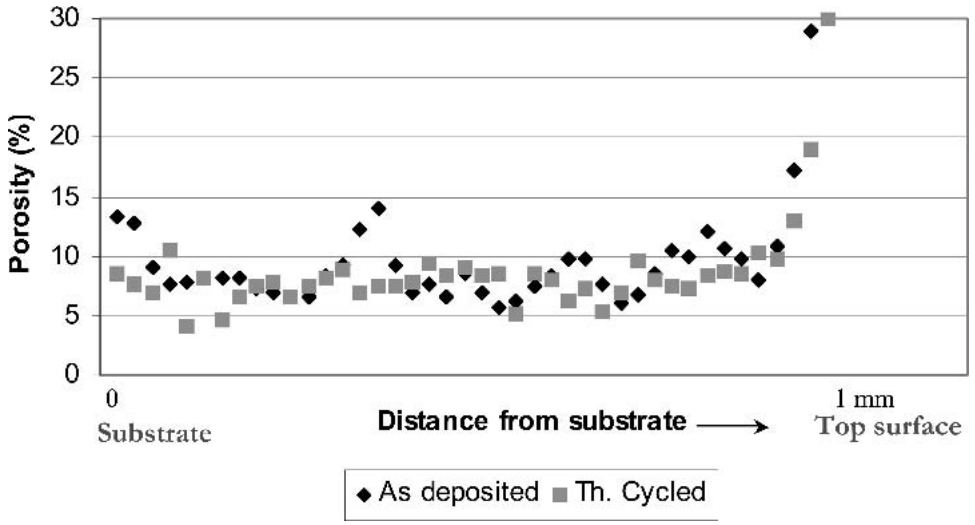

Fig. 10 The effect of thermal cycling on the porosity variation through the coating thickness. The fluctuation in the as-sprayed coating reflects spatial variation in the layered splat structure. After thermal cycling, much of the variation has been sintered out.

variation has disappeared upon thermal cycling. Some degree of sintering of the globular pores is evident in the XMT images; however, the SANS and USAXS results indicate significant sintering of the other voids present, which were not resolved by XMT.

8. Conclusions

Through extension of existing SANS (i.e., MSANS) and USAXS experimental methods, together with a corresponding extension in the interpretation of their data using anisotropic mi-

crostructural models, significant advances have been successfully demonstrated in the microstructural characterization of industrially relevant TBCs.

The distributions of various void defects have been delineated and are related to specific process controls:

- Microstructure and processing parameters have been correlated with coating properties, such as thermal conductivity and elastic modulus.
- This kind of integrated approach, combined with tracing the evolution of microstructural and property changes upon service-encountered heating, is now available to help establish rigorous processing-microstructure-property relationships in future TBC designs.

Acknowledgments

This research was supported by the National Science Foundation MRSEC program at the State University of New York at Stony Brook under grant No. DMR-0080021. This work used facilities supported in part by the National Science Foundation (NSF) under agreement No. DMR-9986442. We acknowledge the support of the NIST, U.S. Department of Commerce, in providing the neutron research facilities used in this work. The authors wish to thank Dr. Sanjay Sampath of the Materials Science Department for valuable discussions, Dr. Brent Lindquist of the Applied Mathematics Department for providing the medial axis code, and Dr. Boualem Hammouda of the NIST Center for Neutron Research, and Dr. Pete Jemian of the Advanced Photon Source (APS) for scientific and technical support. The UNICAT facility at the APS is supported by the University of Illinois at Urbana-Champaign, Materials Research Laboratory (U.S. Department of Energy [DOE], the State of Illinois-IBHE-HECA, and the NSF), the Oak Ridge National Laboratory (U.S. DOE under contract with UT-Battelle LLC), the NIST (U.S. Department of Commerce) and UOP LLC. The APS is supported by the U.S. DOE, Basic Energy Sciences, Office of Science under contract No. W-31-109-ENG-38.

References

1. J.C. Williams, *Materials for Advanced Power Engineering,* D. Coutsouradis, Ed., Kluwer Academic Publishers, Dordrecht, 1994, p 1831
2. W. J. Brindley and R.A. Miller, TBCs for Better Engine Efficiency, *Adv. Mater. Proc.,* Vol 8, 1989, p 29
3. S.M. Meier and D.K. Gupta, The Evolution of Thermal Barrier Coatings in Gas Turbine Applications, *J. Eng. Gas Turbines Power,* Vol 116, 1994, p 250
4. R.L. Jones, Thermal Barrier Coatings, *Metallurgical and Protective Coatings,* K.H. Stern, Ed., Chapman and Hall, London, 1996, p 194
5. W. Mannsmann and H.W. Grunling, Plasma-Sprayed TBC for Industrial Gas Turbines: Morphology, Processing and Properties, *J. Phys IV,* Vol 3, 1993, p 903
6. H. Herman, Plasma-Sprayed Coatings, *Sci. Am.,* Vol 259 (No. 3), 1988, p 112
7. P. Bengtsson, T. Ericsson, and J. Wigren, Thermal Shock Testing of Burner Cans Coated with a Thick Thermal Barrier Coating, *J. Thermal Spray Technol.,* Vol 7 (No. 3), 1998, p 340
8. R. McPherson, The Relationship Between the Mechanisms of Formation, Microstructure and Properties of Plasma-Sprayed Coatings, *Thin Solid Films,* Vol 83, 1981, p 297
9. F. Andreola, C. Leonelli, M. Romagnoli, and P. Miselli, Techniques Used to Determine Porosity, *Am. Ceram. Soc. Bull.,* 2000, p 49
10. D.B. Fowler, W. Riggs, and J.C. Russ, Inspecting Thermal Sprayed Coatings, *Adv. Mater. Proc.,* Vol 11, 1990, p 41
11. K. Mailot, F. Gitzhofer, and M.I. Boulos, Absolute Coating Porosity Measurement Using Image Analysis, *Thermal Spray: Meeting the Challenges of the 21st Century,* Vol 1, C. Coddet, Ed., May 25-29, 1998 (Nice, France), ASM International, 1998, p 917
12. S.T. Bluni and A.R. Marder, The Use of Quantitative Image Analysis for the Characterization of a Thermal Spray Coating, *Thermal Spray Coatings: Properties, Processes and Applications,* T.F. Bernecki, Ed., May 4-10, 1991 (Pittsburgh, PA), ASM International, 1992, p 89
13. A.J. Allen, J. Ilavsky, G.G. Long, J.S. Wallace, C.C. Berndt, and H. Herman, Microstructural Characterization of Yttria-Stabilized Zirconia Plasma-Sprayed Deposits Using Multiple Small-Angle Neutron Scattering, *Acta Mater.,* Vol 49, 2001, p 1661
14. A.J. Allen and N.F. Berk, Analysis of Small-Angle Scattering Data Dominated by Multiple Scattering for Systems Containing Eccentrically Shaped Particles or Pores, *J. Appl. Cryst.,* Vol 27, 1994, p 878
15. A. Kulkarni, Z. Wang, T. Nakamura, S. Sampath, A. Goland, H. Herman, A.J. Allen, J. Ilavsky, G. Long, J. Frahm, and R.W. Steinbrech, Comprehensive Microstructural Characterization and Predictive Property Modeling of Plasma-Sprayed Zirconia Coatings, *Acta Mater.,* Vol 51, 2003, p 2457
16. U. Bonse and M. Hart, A New Tool for Small-Angle X-Ray Scattering and X-Ray Spectroscopy: the Multiple Reflection Diffractometer, *Appl. Phys. Lett.*, Vol 7, 1965, p 238
17. J. Ilavsky, A.J. Allen, G.G. Long, and P.R. Jemian, Effective Pinhole-Collimated Ultrasmall-Angle X-Ray Scattering Instrument for Measuring Anisotropic Microstructures, *Rev. Sci. Instruments,* Vol 73 (No. 3), 2002, p 1660
18. B.A. Dowd, A.B. Andrews, R.B. Marr, D.P. Siddons, K.W. Jones, and A. M. Peskin, Advances in Synchrotron X-Ray Computed Microtomography at the National Synchrotron Light Source, *Adv. X-ray Anal.,* 1999, p 42
19. D. Mancini, F. DeCarlo, Y.S. Chu, and B. Lai, Bending-Magnet Beamline for X-Ray Microtechniques at the Advanced Photon Source, *Rev. Sci. Instruments,* Vol 73 (No. 3), 2002, p 1550
20. W.B. Lindquist, S.M. Lee, D.A. Coker, K.W. Jones, and P. Spanne, Medial Axis Analysis of Void Structure in Three-Dimensional Tomographic Images of Porous Media, *J. Geophys. Res.,* Vol 101 (No. B4), 1996, p 8297
21. W. Oh and W.B. Lindquist, Image Thresholding Using Indicator Kriging, *IEEE Trans. Patt. Anal. Mach. Intell.,* Vol 21, 1999, p 590
22. A. Vaidya, G. Bancke, S. Sampath, and H. Herman, Influence of Process Variables on the Plasma-sprayed Coatings: An Integrated Study, *Thermal Spray 2001: New Surfaces for a New Millennium,* C.C. Berndt, K.A. Khor, and E.F. Lugscheider, Ed., May 28-30, 2001 (Singapore), ASM International, 2001
23. J. Ilavsky, A.J. Allen, G.G. Long, S. Krueger, C.C. Berndt, and H. Herman, Influence of Spray Angle on the Pore and Crack Microstructure of Plasma-Sprayed Deposits, *J. Am. Ceram. Soc.,* Vol 80, 1997, p 733
24. A. Kulkarni, A. Vaidya, A. Goland, S. Sampath and H. Herman, Processing Effects on Porosity-Thermal Conductivity Correlations in Plasma-sprayed Yttria-Stabilized Zirconia Coatings, *Mater. Sci. Eng., A*, Vol 359 (No. 1-2), 2003, p 100
25. J.A. Potton, G.J. Daniell, and B.D. Rainford, Particle Size Distribution from SANS Data Using the Maximum Entropy Method, *J. Appl. Cryst.,* Vol 21, 1988, p 663